Inorganic Chemistry

Article

pubs.acs.org/IC

Photophysical Properties of Endohedral Amine-Functionalized Bis(phosphine) Pt(II) Complexes as Models for Emissive Metallacycles

J. Bryant Pollock,*[,†] Timothy R. Cook,[†] Gregory L. Schneider,[†] Daniel A. Lutterman,[‡] Andrew S. Davies,[†] and Peter J. Stang*[,†]

[†]Department of Chemistry, University of Utah, 315 South 1400 East, RM 2020, Salt Lake City, Utah 84412, United States

[‡]Chemical Sciences Division, Oak Ridge National Laboratory, Oak Ridge, Tennessee 37831, United States

Supporting Information

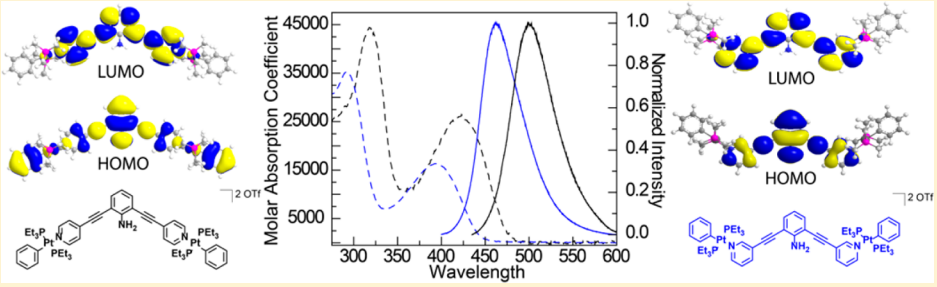

ABSTRACT: The photophysical properties of bis(phosphine) Pt(II) complexes constructed from 2,6-bis(pyrid-3-ylethynyl) aniline and 2,6-bis(pyrid-4-ylethynyl) aniline vary significantly, even though the complexes differ only in the position of the coordinating nitrogen. By capping the ligands with an aryl bis(phosphine) Pt(II) metal acceptor, the photophysical properties of the two isomeric systems were directly compared, revealing that the low-energy absorption and emission bands of the two systems were separated by 30 nm (1804 cm^{-1}) and 39 nm (1692 cm^{-1}), respectively. From the analysis of time-dependent density functional (TD-DFT) calculations and excited-state lifetime measurements, it was determined that the nature of the Pt−N bond in the HOMO and the sums of the radiative (k_{rad}) and nonradiative (k_{nr}) rate constants were significantly different in the two systems. As the dominant nonradiative decay pathway in aniline systems is relaxation from the triplet state through intersystem crossing (ISC), the difference in k_{nr} can be ascribed to changes in ISC between isomers of the bis(phosphine) Pt(II)-capped 2,6-bis(pyrid-3-ylethynyl) aniline system. It was also determined that the photophysical properties of these capped systems can be altered by functionalizing the aryl capping ligand on the bis(phosphine) Pt(II) metal center, which perturbs the molecular orbitals involved in the observed optical transitions. In addition, an isoelectronic bis(phosphine) Pd(II)-capped system was prepared for comparison with the bis(phosphine) Pt(II) suite of complexes. The Pd(II) system showed significant changes in its low-energy absorption band, but preserved the characteristic emissive properties of its Pt(II) analogue with an even higher quantum yield.

INTRODUCTION

Transition-metal-mediated coordination-driven self-assembly has blossomed over the past two decades, leading to increasingly complex systems with multiple functionalizations and various shapes and volumes for host−guest encapsulation, catalysis, and biomedical applications.[1] The Stang group has pioneered a strategy called the directional-bonding approach whose archetypal construction method utilizes bis(phosphine) Pt(II) metal nodes and pyridyl-based organic spacers; each component has encoded directionality and angularity that dictates the architectural outcome.[2] Fundamental studies on the photophysical properties of Pt-based supramolecular coordination complexes (SCCs), such as polygons, are rare and warrant attention if these systems are to realize their promising potential for applications in photon-emitting devices or bioimaging.[3]

The well-established photophysical properties of mono- and multinuclear bis(phosphine)platinum coordination complexes (e.g., low-energy and long-lived excited states, facile tunability, and high quantum yields) have set the foundation for studying SCCs constructed using bis(phosphine)platinum metal centers that can preserve these useful absorption and emission characteristics.[4] Recently, a D_{2h} [2 + 2] endohedral amine-functionalized rhomboid (**8**, Scheme 1) constructed from 2,6-bis(pyrid-4-ylethynyl) aniline (**1**, Scheme 1) and 2,9-bis[*trans*-$Pt(PEt_3)_2NO_3$] phenanthrene[5] that displayed a low-energy absorption band in the visible region and emitted above 500 nm was reported.[6] The emissive properties were attributed to ligand-centered transitions involving π-type molecular orbitals with modest contributions from metal-based atomic orbitals.

Received: February 25, 2013

   dx.doi.org/10.1021/ic400491q | *Inorg. Chem.* XXXX, XXX, XXX−XXX

Scheme 1. Systems for investigating the effects of structural isomerism

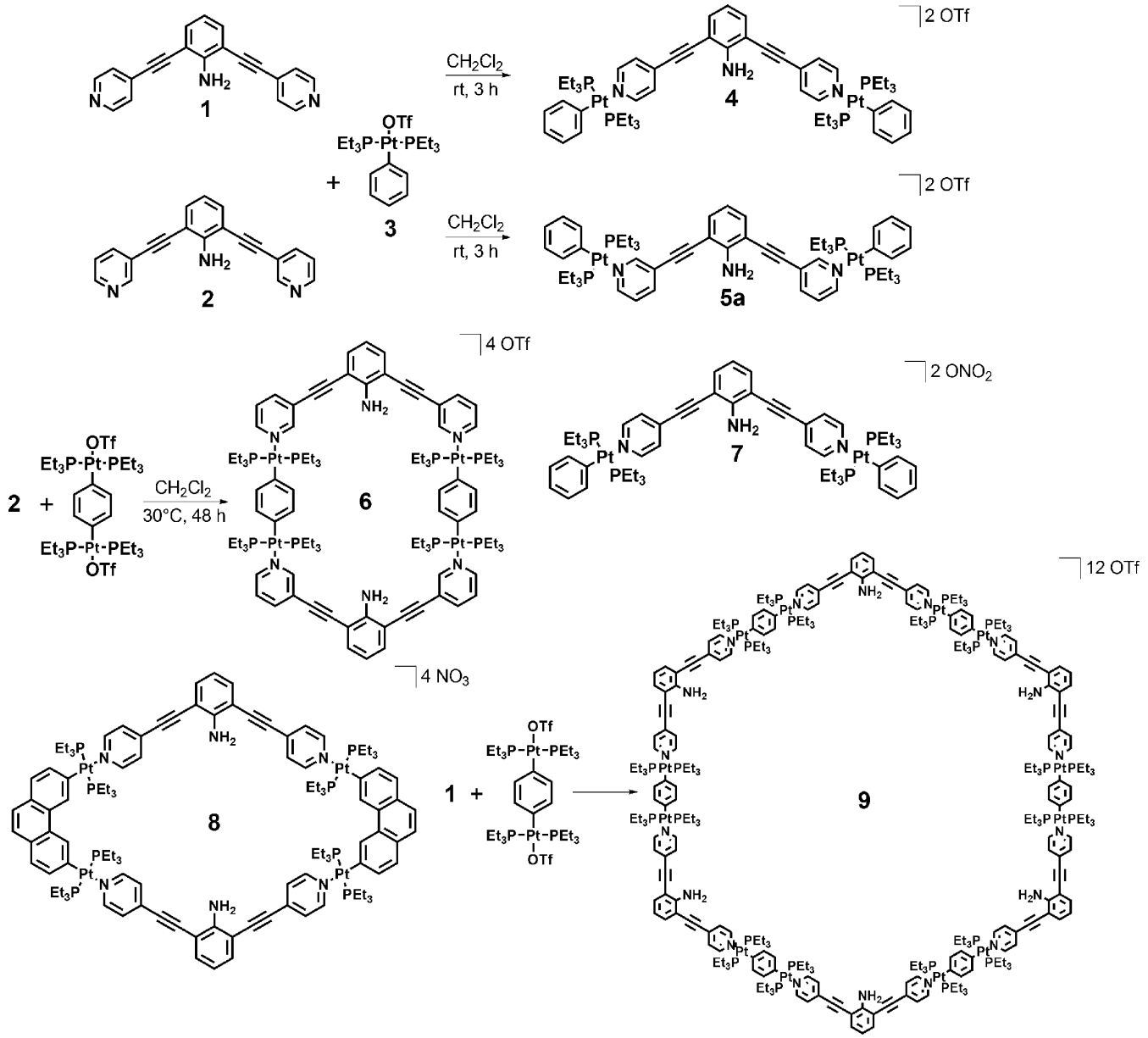

Further investigations of these systems are critical for designing SCCs that exhibit the attractive photophysical properties established for mono- and multinuclear bis(phosphine) platinum coordination complexes.

Investigations probing the effects of size and shape on the photophysical properties of Pt-based SCCs are relatively rare when compared to synthetic and structural studies.[3a] For instance, although it is clear that the position of the coordinating nitrogen dictates the architectural outcome of a self-assembly, the photophysical ramifications of structural isomerism are not well understood. Here, we employ two isomeric ligands: the previously mentioned 120° 2,6-bis(pyrid-4-ylethynyl) aniline[5] donor (**1**), which has the coordinating nitrogen *para* to the ethynyl moiety, and 2,6-bis(pyrid-3-ylethynyl) aniline[7] (**2**), which, with its nitrogen meta to the ethynyl moiety, represents a cliplike 0° donor (Scheme 1). Because the different angularities of donors **1** and **2** necessarily obviate the ability to form structurally analogous SCCs, a platinum acceptor (**3**) was synthesized to effectively cap each ligand. Given that the photophysical properties of the aforementioned rhomboidal SCC containing **1** were attributed to ligand-centered transitions, it was anticipated that the emissive behavior of such SCCs could be largely preserved in model systems wherein a ligand is capped by two Pt centers, truncating a metallacycle to a single Pt−ligand−Pt fragment. As models of the Pt−ligand−Pt fragment of SCCs, **4** and **5a** reveal the effects of structural isomerism for ligands commonly used in metallacycle formation (Scheme 1).[3a] Although **5a** can exist as two additional conformers, the configuration shown in Scheme 1 is the energetic minimum as indicated by density functional theory (DFT) calculations (vide infra). Interestingly, the nature of the molecular orbitals involved with the low-energy optical transition for **4** are significantly different from that of the previously reported system.

It has been established that the molecular orbitals involved with the observed optical transitions from endodedral amine-functionalized systems arise from mainly ligand-centered transitions, with only modest contributions from the metal

dx.doi.org/10.1021/ic400491q | *Inorg. Chem.* XXXX, XXX, XXX−XXX

Scheme 2. Systems for probing the effects of the metal-containing fragments

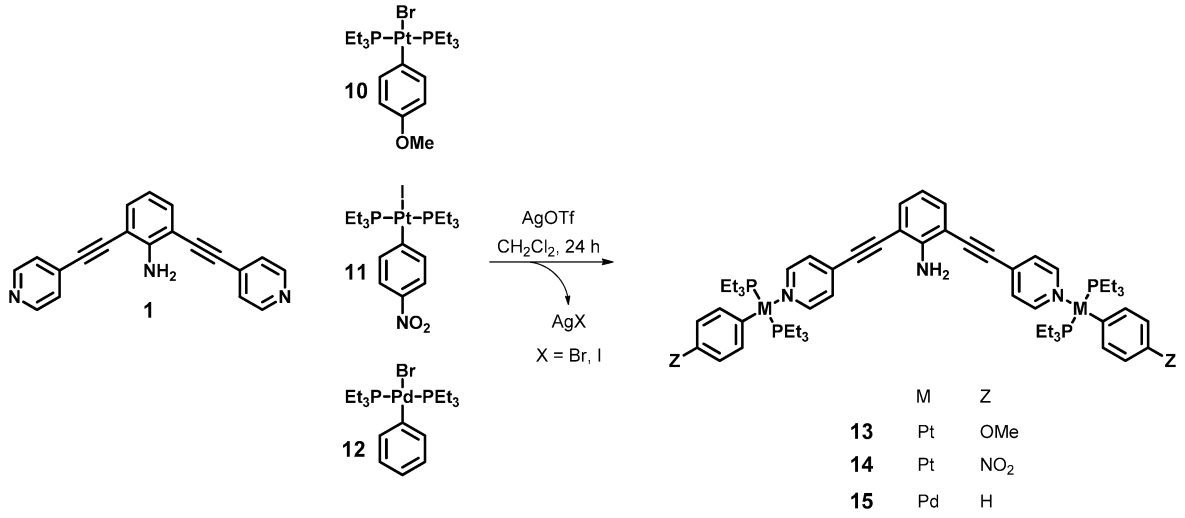

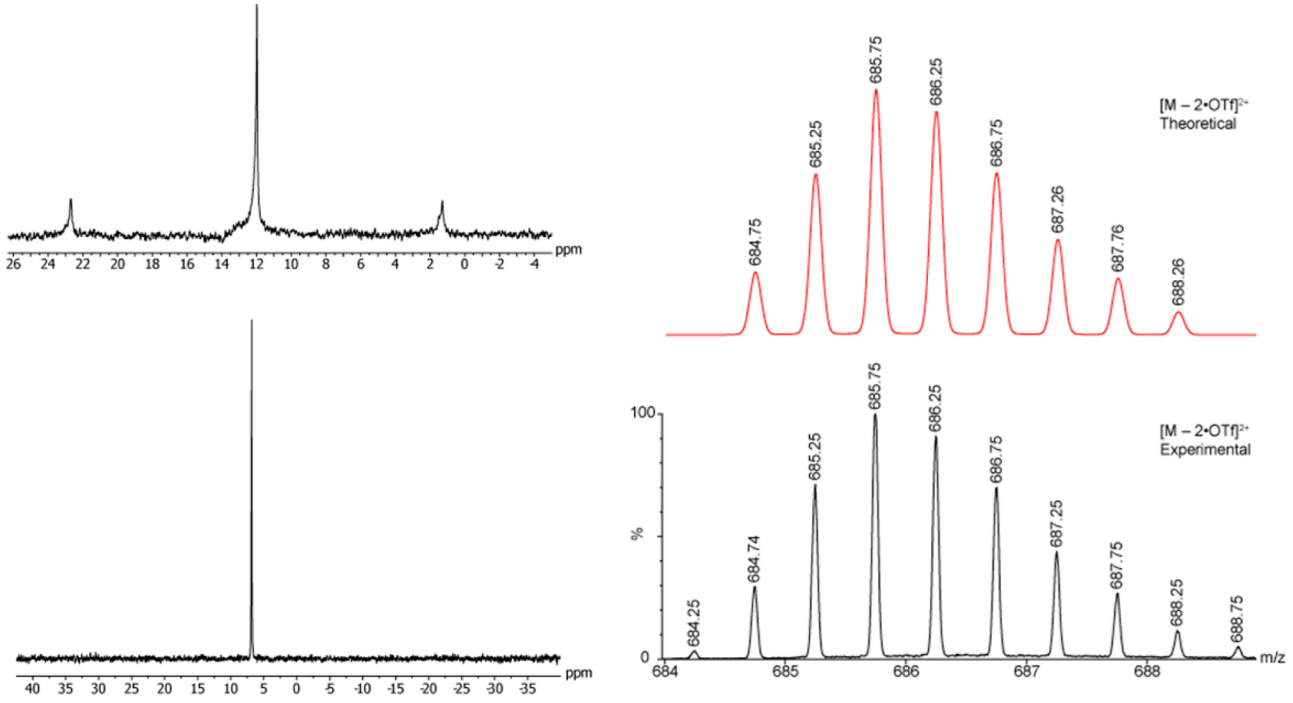

Figure 1. $^{31}P\{^{1}H\}$ NMR spectra of **14** (left, top) and **15** (left, bottom) and ESI mass spectrum of **13** (right).

center; despite the lack of metal character in the orbitals involved in allowed electronic transitions, complexation of the dipyridyl ligands gives marked spectral shifts, as high as 100 nm (4540 cm^{-1}) when **1** coordinates to Pt.[6] As such, a complementary suite of compounds was synthesized to probe the photophysical influence stemming from the metal-containing fragment of these model systems. To accomplish this, the trans aryl group on the bis(phosphine) Pt(II) metal center was functionalized with either a methoxy group (**13**, Scheme 2) or a nitro group (**14**, Scheme 2). These molecules were investigated using computational methods to determine the origins of any observed spectral changes. Also, an isoelectronic bis(phosphine) Pd(II) analogue of **4** (**15**, Scheme 2) was prepared to answer the following questions: (i) Can ISC be attenuated using a metal less prone to exhibit spin−orbit coupling, thus circumventing the main nonradiative decay pathway of these aniline compounds? (ii) Are desirable photophysical properties (visible wavelength emission, tunable bands, etc.) retained when using a second-row d^8 metal center versus a third-row d^8 Pt(II) metal center? Herein, the synthesis and steady-state absorption and emission and excited-state lifetime measurements of these SCC model systems are described with the intention of establishing the effects of structural isomers and effects originating from the perturbations of the electronics of the metal nodes by incorporating auxiliary functional groups on the bis(phosphine) aryl Pt(II) capping unit and substituting Pt(II) for Pd(II) metal centers. These experiments were augmented by DFT and time-dependent DFT (TD-DFT) calculations to probe the nature of the observed optical transitions.

dx.doi.org/10.1021/ic400491q | *Inorg. Chem.* XXXX, XXX, XXX−XXX

Table 1. Photophysical Data of Compounds 4, 5a, and 6−9

compound	absorption bands λ_{max} (nm) [$\varepsilon \times 10^{-3}$ (cm^{-1} M^{-1})]	λ_{exc} (nm)	λ_{emiss} (nm)	Φ^a (%)	τ (10^{-9} s)	$k_{rad}{}^b$ (10^8 s^{-1})	$k_{nr}{}^b$ (10^8 s^{-1})
1[c]	282 [28.6], 300 sh [20.7], 373 [13.7]	356	422	65	2.55	2.55	1.37
2	300 sh [17.7], 362 [12.2]	365	408	30	2.59	1.16	2.70
4	318 [44], 423 [26]	423	500	32	1.37	2.34	4.96
5a	292 [35], 393 [16]	393	461	19	2.58	0.74	3.14
6	293 [16], 402 [10]	402	466	12			
7	321 [36], 425 [20]	425	510	34			
8[c]	258 [135], 267 sh [130], 288 [85.2], 317 [112], 430 [39.9]	430	522	28			
9[c]	284 sh [95.2], 318 [139], 422 [87.6]	422	505	15			

[a]Quinine sulfate at 365 nm was used for quantum yield determination. [b]$k_{rad} = \Phi\tau^{-1}$, $k_{nr} = \tau^{-1} - k_{rad}$. [c]Absorption and quantum yield data obtained from ref 6.

RESULTS

Synthesis. The Pt-capped dipyridyl aniline compounds in Scheme 1 were obtained under synthetic conditions similar to those used for SCC formation. A CH_2Cl_2 solution of **1** or **2** with **3**, reflecting the 2:1 stoichiometry of acceptor to donor, furnished the Pt−ligand−Pt triads after 3 h of stirring at room temperature and precipitation by diethyl ether. The combination of **2** and a linear diplatinum donor[8] in a 1:1 ratio extends the Pt−ligand−Pt motif to a closed metallacycle, **6**, which was used to validate **5a** as an appropriate model for larger SCCs. Similarly, the combination of **1** with the linear donor furnished hexagonal metallacycle **9**[6] whose properties were useful in comparison to model system **4**. These systems were characterized through electrospray ionization mass spectrometry (ESI-MS) and $^{31}P\{^1H\}$ and ^1H NMR spectrometry (Figures S1−S23, Supporting Information).

The M−ligand−M triads in Scheme 2 (**13−15**) were synthesized by stirring **1** with **10**,[9] **11**,[10] or **12**[11] in 1:2 stoichiometry with 2 equiv of silver triflate in CH_2Cl_2. After 24 h of stirring at room temperature in the dark, the solutions were filtered to remove insoluble silver halide. Diethyl ether was then added to the homogeneous solution to precipitate the product. The solids were then dried overnight in vacuo and redissolved in CD_2Cl_2 for characterization (Figures S24−S39, Supporting Information). Figure 1 displays the $^{31}P\{^1H\}$ NMR spectra of **14** (top left) and **15** (bottom left), where the loss of ^{195}Pt satellites for **15** is evident. The electrospray ionization mass spectrum of the doubly charged $[M - 2OTf]^{2+}$ ion for **13** is shown in Figure 1 (right) and is in good agreement with the theoretical isotopic distribution pattern (shown in red). In each case, a characteristic downfield shift of the pyridyl protons was observed upon coordination to the metal centers.

Photophysical Properties. As reported in Table 1, ligands **1** and **2** were determined to have low-energy absorption bands centered at 373 and 362 nm, respectively, with similar molar absorption coefficients (**1**, 13700 cm^{-1} M^{-1}; **2**, 12200 cm^{-1} M^{-1}). A single emission band was observed for **1** and **2**, centered at 422 and 408 nm, respectively. The quantum yield of **1** (Φ = 65%) was roughly twice that of **2** (Φ = 30%).

Figure 2 displays the absorption and emission spectra of **4**−**7**, with the relevant metrics summarized in Table 1. Each compound is characterized by a high-energy absorption band between 300 and 350 nm, with the largest molar absorption coefficient being observed for **4**. In addition, all four species exhibited a less intense band at longer wavelengths of ∼400−450 nm. The molar absorption coefficients of the second bands (∼10000−25000 cm^{-1} M^{-1}) are roughly half those of the higher-energy bands (∼15000−45000 cm^{-1} M^{-1}).

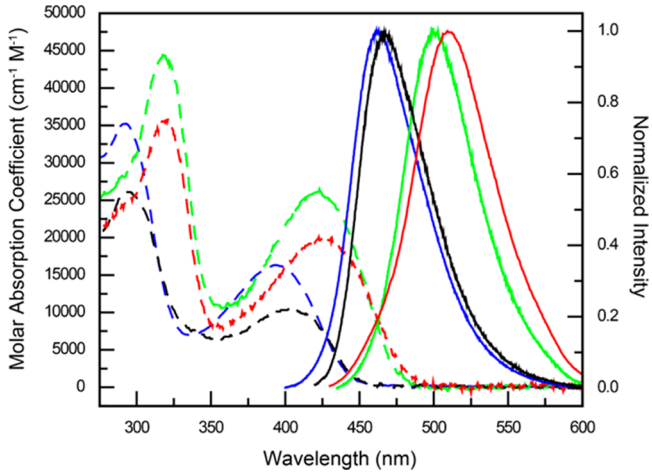

Figure 2. Absorption (dashed) and emission (solid) spectra of **4** (green), **5a** (blue), **6** (black), and **7** (red). The spectra were collected in aerated CH_2Cl_2 at room temperature.

The single emission bands for this series of compounds are centered at 500 nm for **4**, 461 nm for **5a**, 466 nm for **6**, and 510 nm for **7** with corresponding quantum yields (Φ) of 32%, 19%, 12%, and 34%, respectively.

Excited-state lifetime measurements were performed using an 800 ps pulse width excitation at 336 nm. The decay of the excited state was monitored by the loss of emission intensity at the wavelength maximum for each sample, as determined from steady-state measurements. The decay profiles were fit to biexponential functions where τ_1 corresponded to the intact platinated species of **4** (1.37 ns) and **5a** (2.58 ns), with 83.6% and 97.7% contributions, respectively. All excited-state lifetime traces can be found in Figure S39 (Supporting Information).

Figure 3 displays the absorption and emission spectra of **13**−**15**, with the relevant metrics summarized in Table 2. Each compound is characterized by a high-energy band between 306 and 325 nm, with the largest molar absorption coefficient being observed for **14**. In addition, all species contain a less intense band at longer wavelengths of ∼400−425 nm. The molar absorption coefficient of the higher-energy band (∼35000−65000 cm^{-1} M^{-1}) is roughly twice that of the low-energy band (∼20000−23000 cm^{-1} M^{-1}).

The single emission bands for this series of compounds were centered at 500 nm for **13**, 508 nm for **14**, and 494 nm for **15** with quantum yields (Φ) of 20%, 13%, and 41%, respectively.

The effect of excitation wavelength on the lifetimes of **13**−**15** was investigated by employing both 336 and 458 nm light in the measurements to determine whether the lifetime was independent of wavelength. The decay profiles were fit to

dx.doi.org/10.1021/ic400491q | Inorg. Chem. XXXX, XXX, XXX−XXX

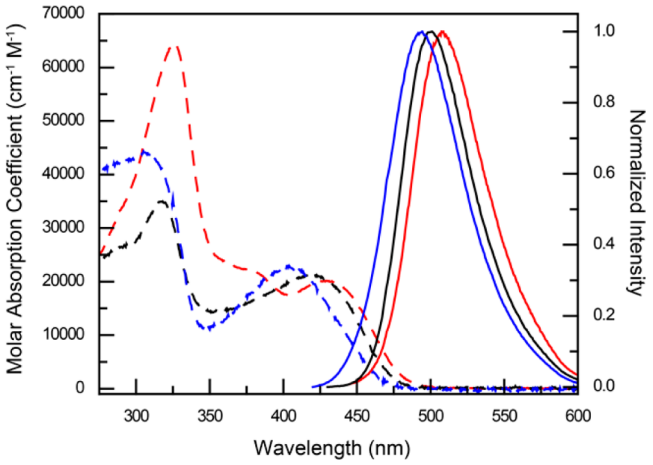

Figure 3. Absorption (dashed) and emission (solid) spectra of **13** (black), **14** (red), and **15** (blue). The spectra were collected in aerated CH_2Cl_2 at room temperature.

Table 2. Photophysical Data of Compounds 13−15

compound	absorption bands λ_{max} (nm) [$\varepsilon \times 10^{-3}$ (cm^{-1} M^{-1})]	λ_{exc} (nm)	λ_{em} (nm)	Φ^a (%)	τ (10^{-9} s)	$k_{rad}{}^b$ (10^8 s^{-1})	$k_{nr}{}^b$ (10^8 s^{-1})
13	317[35], 420 [21]	420	500	20	2.20	0.91	3.64
14	325 [65], 377 sh [22], 429 [20]	429	508	13	2.62	0.50	3.32
15	306 [44], 404 [23]	404	494	41	3.26	1.26	1.81

[a]Quinine sulfate at 365 nm was used for quantum yield determination. [b]$k_{rad} = \Phi\tau^{-1}$, $k_{nr} = \tau^{-1} - k_{rad}$.

biexponential functions where the average of the τ_1 value corresponded to the intact platinated species of **13** (2.20 ns) and **14** (2.62 ns) and the palladium-bound **15** (3.26 ns) with 95.8%, 95.5%, and 88.5% contributions, respectively, at 336 nm. Similar lifetimes were observed at 458 nm (Table S2, Supporting Information), indicating that the excited state leading to radiative decay is accessed through internal conversion and is thus independent of the wavelength of excitation.

Photophysical Discussion. It is readily apparent that the position of the pyridyl nitrogen atom has an effect on the resulting photophysical properties of **1** and **2**, as evidenced by the red-shifted low-energy absorption and emission band maxima of **1** (373 and 422 nm, respectively) when compared to those of **2** (362 and 408 nm, respectively). The quantum yield of **1** (Φ = 65%) was determined to be more than twice that of **2** (Φ = 30%). It should be noted that previous reports have determined that the main nonradiative decay pathway from the S_1 excited state of aniline-based compounds is through ISC to a nonradiative triplet state.[12]

Interestingly, upon platination, ligands **1** and **2** have marked shifts in the low-energy absorption and emission bands. Comparing ligand **1** to complex **4**, the low-energy absorption band maximum is red-shifted by 50 nm (3169 cm^{-1}), and the emission band maximum is red-shifted by 78 nm (3697 cm^{-1}). Similarly, but to a lesser degree, the low-energy absorption and emission band maxima of **2** are red-shifted when compared to **5a** by 31 nm (2179 cm^{-1}) and 53 nm (2818 cm^{-1}), respectively. An overall loss of quantum yield was also observed upon platination with **4** (Φ = 32%) being 33% lower than that of **1**, whereas **5a** (Φ = 19%) is 11% lower than that of **2**.

The apparent differences in the photophysical properties that arise from the position of the pyridyl nitrogen atom in ligands **1** and **2** are preserved when comparing **4** and **5a**, as evidenced by the blue shift of the low-energy absorption and emission peak maxima of **5a** (30 and 39 nm, or 1804 and 1692 cm^{-1}, respectively) when compared to those of **4**. In addition, the molar absorption coefficient for the low-energy absorption band was 16000 cm^{-1} M^{-1} (393 nm) for **5a** but was less than that of **4** at 26000 cm^{-1} M^{-1} (423 nm).

The photophysical differences between isomers **4** and **5a** were further manifested in the quantum yields, as that of **5a** (Φ = 19%) is lower than that of **4** (Φ = 32%). To better understand these differences, excited-state lifetime measurements were employed to probe the radiative and nonradiative rate constants of the excited state.

The excited-state lifetimes (τ_1) of **1** (2.55 ns), **2** (2.59 ns), **4** (1.37 ns), and **5a** (2.58 ns) are all similar in magnitude, as are the rate constants for the radiative decay pathway of **1** (k_{rad} = 2.55 × 10^8 s^{-1}) and **4** (k_{rad} = 2.34 × 10^8 s^{-1}), which were calculated using the quantum yields and excited-state lifetimes. However, the rate constant for the nonradiative decay pathway for **4** (k_{nr} = 4.96 × 10^8 s^{-1}) is more than twice that of **1** (k_{nr} = 1.37 × 10^8 s^{-1}). Because k_{nr} is the sum of the rate constants for all nonemissive processes, this indicates that **4** either has access to more nonradiative decay pathways or has better overlap with a nonradiative excited state; moreover, the inclusion of platinum in these systems enhances the rate of spin-forbidden processes, coined the "heavy-atom effect". From the TD-DFT

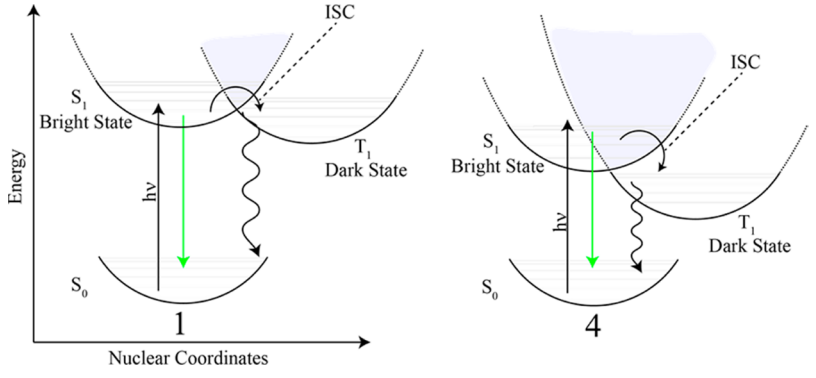

Figure 4. Jablonski diagrams for **1** (left) and **4** (right).

dx.doi.org/10.1021/ic400491q | Inorg. Chem. XXXX, XXX, XXX−XXX

calculations (vide infra), it was determined that **4** utilizes the frontier orbitals during the lowest-energy electronic transition. Therefore, although it is advantageous in some Pt-based systems to increase ISC,[4d,13] the decrease in the quantum yield of **4** (Φ = 32%) when compared to that of **1** (Φ = 65%) could be attributed to better overlap between the nonradiative triplet and S_1 excited states (shown in Figure 4); no phosphorescence was observed in the platinated species in degassed, oxygen-free solvent. Interestingly, the rate constants for the radiative decay pathways for **2** ($k_{rad} = 1.16 \times 10^8$ s^{-1}) and **5a** ($k_{rad} = 0.74 \times 10^8$ s^{-1}) are different, indicating that platination not only induces ISC, as was seen in the case of **1** versus **4**, but also affects the radiative decay pathway.

The rate constants for the radiative and nonradiative decay pathways of **4** ($k_{rad} = 2.34 \times 10^8$ s, $k_{nr} = 4.96 \times 10^8$ s^{-1}) are higher than those of **5a** ($k_{rad} = 0.74 \times 10^8$ s^{-1}, $k_{nr} = 3.14 \times 10^8$ s^{-1}), which implies that the higher quantum yield of **4** is due to ligand **1** (Φ = 65%) when compared to **2** (Φ = 30%). Also, the quantum yield of **4** (Φ = 32%) is one-half that of **1** (Φ = 65%), whereas the quantum yield of **5a** (Φ = 19%) is two-thirds that of **2** (Φ = 30%). Understanding these differences requires an analysis of the molecular orbitals involved in the relevant optical transitions (vide infra).

Platinum complexes **4** and **5a** were then compared to metallacyclic SCC analogues to evaluate the use of capped M−L−M fragments as models for larger systems. Because computational investigations implicate ligand-centered highest occupied molecular orbital (HOMO) and lowest unoccupied molecular orbital (LUMO) in the low-energy optical transitions of **4** and **5a** (vide infra), it was expected that these truncated fragments were valid models.

Comparing **5a** to its hexagonal SCC counterpart, **6**, the low-energy absorption and emission bands of **5a** are blue-shifted by 9 nm (569 cm^{-1}) and 5 nm (233 cm^{-1}), respectively. The quantum yield of **5a** (Φ = 19%) is higher than that of **6** (Φ = 12%). The absorption and emission profiles are in good agreement for **5a** versus **6**, and the quantum yield difference can be explained by the inclusion of more Pt(II) metal centers, which will enhance the heavy-atom effect. Therefore, **5a** is a good model for **6**.

The previously reported endohedral amine-functionalized D_{2h} [2 + 2] rhomboid (**8**, Scheme 1) synthesized from ligand **1** and a 60° phenanthrene diplatinum nitrate acceptor (Scheme 1) has photophysical properties that show relatively greater discrepancies from those of **4**. The low-energy absorption and emission peak maxima of **8** are both blue-shifted by 7 nm (385 cm^{-1}) and 22 nm (843 cm^{-1}), respectively. However, when compared to the endohedral amine-functionalized [6 + 6] hexagon[6] (**9**, Scheme 1), which contains ligand **1** and a 180° benzene-based diplatinum triflate acceptor, the low-energy absorption bands differs by only 1 nm (56 cm^{-1}), and the emission band of **9** is red-shifted by 5 nm (198 cm^{-1}) relative to that of **4**; the shifts in the observed optical transitions are thought to arise from the differences in the aromatic scaffolds (i.e., **3** has a benzene core scaffold much like the 180° benzene-based diplatinum acceptor, whereas the rhomboid is synthesized from a 60° phenanthrene-based diplatinum acceptor). As such, **4** appropriately models the photophysical properties of its analogous hexagonal SCC, but not its rhomboidal counterpart.

To probe the differences in the photophysical properties of **4** and **8**, the counterion and the aromatic group trans to the coordinating nitrogen were investigated. The nitrate counterion analogue of **4** (**7**, Scheme 1) was prepared and foundto exhibit low-energy absorption and emission peak maxima that were red-shifted when compared to those of **4** by 2 nm (112 cm^{-1}) and 10 nm (392 cm^{-1}), respectively. This result is interesting because the counterions of an SCC are often thought to be outer-sphere and typically are not ascribed any photophysical relevance. Also, the low-energy absorption and emission peak maxima of **7** are blue-shifted by 5 nm (273 cm^{-1}) and 12 nm (451 cm^{-1}), respectively, when compared to those of **8**, which indicates that these systems are sensitive to the nature of the aryl group trans to the Pt−N.

To better understand and probe this effect, the aryl group trans to the coordinating nitrogen was functionalized at the para position to give systems with an electron-donating methoxy group (**13**, Scheme 2) and an electron-withdrawing nitro group (**14**, Scheme 2). Previous studies hypothesized that π back-bonding from the bis(phosphine) Pt(II) metal center to the coordinated pyridyl nitrogen accounted for the observed optical shifts between free ligands and their coordinated counterparts.[6,14,15] These two compounds allowed for a direct probe into the effects of perturbing the π system of the metal fragments. An isoelectronic bis(phosphine) Pd(II) metal complex (**15**, Scheme 2) was also utilized to attenuate spin−orbit coupling, thereby decreasing the ISC. Because ISC is a known nonradiative decay pathway for aniline-based compounds, this should result in a higher quantum yield.

The NO_2-aryl Pt system (**14**) displayed the lowest-energy absorption (429 nm) and emission (508 nm) band maxima, which were red-shifted when compared to both the non-functionalized aryl system, **4** (λ_{abs} = 423 nm, λ_{em} = 500 nm) and OMe-aryl Pt system **13** (λ_{abs} = 420 nm, λ_{em} = 500 nm). The quantum yield, however, of system **14** (Φ = 13%) is lower than those of **13** (Φ = 20%) and **4** (Φ = 32%), whereas the excited-state lifetime of **14** (τ = 2.62 ns) is higher than those of **13** (τ = 2.20 ns) and **4** (τ = 1.37 ns). From these results, it was calculated that the rate constants for the nonradiative (k_{rad}) and radiative (k_{nr}) decay pathways for **14** ($k_{rad} = 0.50 \times 10^8$ s^{-1}, $k_{nr} = 3.32 \times 10^8$ s^{-1}) were the lowest as compared to those of **13** ($k_{rad} = 0.91 \times 10^8$ s^{-1}, $k_{nr} = 3.64 \times 10^8$ s^{-1}) and of **4** ($k_{rad} = 2.34 \times 10^8$ s^{-1}, $k_{nr} = 4.96 \times 10^8$ s^{-1}).

Pd-based **15** displays a blue shift in both the absorption and emission bands as compared to its isoelectronic Pt-based system, **4**. The low-energy absorption band of **15** was blue-shifted by 19 nm (1111 cm^{-1}), and the emission band maximum was blue-shifted by 6 nm (243 cm^{-1}) when compared to those of **4**. The excited-state lifetime, however, was much higher for **15** (τ = 3.26 ns) than for **4** (τ = 1.37 ns), which could account for the overall 9% higher quantum yield of the former over the latter. For **15**, we calculated $k_{rad} = 1.26 \times 10^8$ s^{-1} and $k_{nr} = 1.81 \times 10^8$ s^{-1}, and the values calculated for **4** were $k_{rad} = 2.34 \times 10^8$ s^{-1} and $k_{nr} = 4.96 \times 10^8$ s^{-1}. The difference in k_{rad} value implies that a different radiative pathway (i.e., the nature of the molecular orbitals involved in the electronic transition) might exist. Therefore, to better understand why the observed optical transitions were higher in energy for **15** when compared to **4**, time-dependent density functional theory (TD-DFT) calculation were employed (vide infra).

DFT and TD-DFT General Information. Geometry optimization calculations were performed using a split basis set where the Becke three-parameter hybrid exchange and the Lee−Yang−Parr correlation functionals (B3LYP)[16] and 6-31G** basis set[17] were used for C, H, N, and P atoms, whereas the Los Alamos National Laboratories 2 Double Zeta

dx.doi.org/10.1021/ic400491q | Inorg. Chem. XXXX, XXX, XXX−XXX

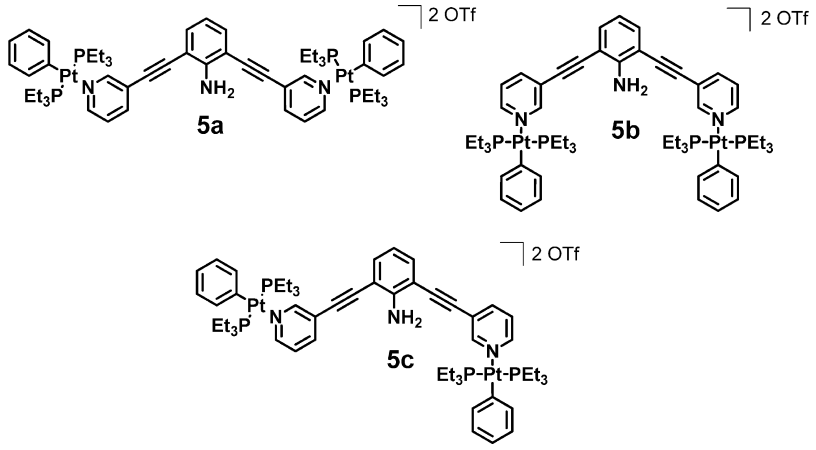

Figure 5. Two additional conformers of **5a** that are possible.

(LANL2DZ)[18] basis set and pseudopotential were used for Pt and Pd. To minimize computational costs, $P(CH_3)_3$ ligands were utilized instead of PEt_3; therefore, the model used to approximate compound **X** is abbreviated as **X**−$P(CH_3)_3$, where **X** is the compound number. A frequency analysis was also performed to determine whether any imaginary states existed below the energy minimum. The vertical singlet transition energies of the complexes were computed by time-dependent density functional theory within Gaussian 09[19] using the ground-state optimized structure. For the structures that were calculated, 1000 or more total molecular orbitals were observed, and each molecular orbital number that is listed is real and in its absolute energetic order. The nomenclature utilized to discuss these molecular orbitals is relative to the HOMO and LUMO (i.e., HOMO−1 is the molecular orbital directly below the HOMO).

As mentioned previously, compound **5a** can exist as one of three conformers as shown in Figure 5. DFT optimizations of the three compounds determined that **5a**−$P(CH_3)_3$ is the lowest in energy (Table 3) by 3.70 kcal/mol when compared to **5b**−$P(CH_3)_3$ and 1.51 kcal/mol when compared to **5c**−$P(CH_3)_3$; therefore, even though the conformers have energies that are very closely related, configuration **5a**−$P(CH_3)_3$ was used in subsequent TD-DFT calculations.

Table 3. DFT Optimization Energies for 5a−$P(CH_3)_3$−5c−$P(CH_3)_3$

compound	energy (hartrees)	Δ (kcal/mol)
5a−$P(CH_3)_3$	−3480.00293429	0.0000
5b−$P(CH_3)_3$	−3479.99704283	3.6970
5c−$P(CH_3)_3$	−3480.00052333	1.5129

TD-DFT Results and Discussion. From the TD-DFT calculations of **4**−$P(CH_3)_3$ and **5a**−$P(CH_3)_3$ (see Table 4), the low-energy optical transitions were determined to originate from a HOMO-to-LUMO electronic transition that involves ligand-centered molecular orbitals with π-type symmetry (Figure 6). The predicted observed low-energy optical transitions occur at 451 nm for **4**−$P(CH_3)_3$ and 424 nm for **5a**−$P(CH_3)_3$. In the low-energy transition for both **4**−$P(CH_3)_3$and **5a**−$P(CH_3)_3$, the HOMO has the nitrogen p orbital and ethynyl π system in phase and bonding, whereas the LUMO has little electron density on the aniline nitrogen p orbital and an antibonding ethynyl π system; however, despite sharing similar characteristics, **4**−$P(CH_3)_3$ also has a significant amount of charge-transfer character. After performing a population analysis, it was determined that, in the HOMO for **4**−$P(CH_3)_3$, 8% of the electron density is on the Pt-phosphine metal center and 15% of the electron density is on benzyl group, whereas 5% and 0.1% of the electron density lie on the Pt-phosphine and benzyl group, respectively, in the LUMO. The ligand gains an appreciable amount of electron density during the HOMO- (77%) to-LUMO (95%) transition, which leads to the charge transfer being described as a mixture of metal−ligand (MLCT) and ligand−ligand (LLCT) charge transfer; the charge-transfer character of the low-energy transition could explain why the emission of **4** is sensitive to the nature of the aromatic group trans to the coordinating N atom of the pyridyl group. Also, for the HOMO of **5a**−$P(CH_3)_3$ (Figure 6, left), the coordinating nitrogen and

Table 4. Electronic Transitions Predicted for 4−$P(CH_3)_3$ and 5a−$P(CH_3)_3$ with $f > 0.2$

compound	wavelength (nm)	orbital transitions	orbital transitions	oscillator strength, f	description
4−$P(CH_3)_3$	451	219 → 220	HOMO → LUMO	0.925	MLCT LLCT $^1\pi \rightarrow {}^1\pi^*$
	343	214 → 221	HOMO−5 → LUMO + 1	1.200	ILCT $^1\pi \rightarrow {}^1\pi^*$
5a−$P(CH_3)_3$	424	219 → 220	HOMO → LUMO	0.715	ILCT $^1\pi \rightarrow {}^1\pi^*$
	329	214 → 221 216 → 221	HOMO−5 → LUMO + 1 HOMO−3 → LUMO + 1	0.746	LLCT LMCT $^1\pi \rightarrow {}^1\pi^*$

dx.doi.org/10.1021/ic400491q | Inorg. Chem. XXXX, XXX, XXX−XXX

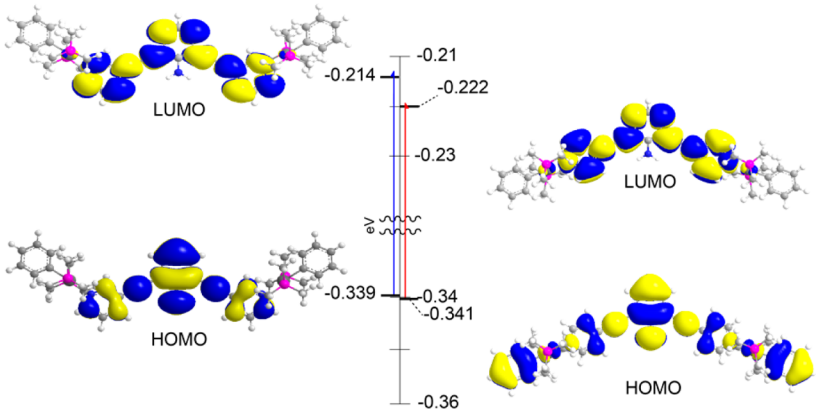

Figure 6. HOMOs and LUMOs of **4**–$P(CH_3)_3$ (right) and **5a**–$P(CH_3)_3$ (left).

Table 5. Electronic Transitions Predicted for 13–$P(CH_3)_3$, 14–$P(CH_3)_3$, and 15–$P(CH_3)_3$ with f > 0.2

compound	wavelength (nm)	orbital transitions	orbital transitions	oscillator strength, f	description
13–$P(CH_3)_3$	447	233 → 236	HOMO−2 → LUMO	0.839	ILCT $^1\pi \rightarrow {}^1\pi^*$
	343	230 → 237	HOMO−5 → LUMO + 1	1.316	ILCT $^1\pi \rightarrow {}^1\pi^*$
	336	230 → 236	HOMO−5 → LUMO	0.253	ILCT
		233 → 237	HOMO−2 → LUMO + 1		$^1\pi \rightarrow {}^1\pi^*$
14–$P(CH_3)_3$	455	241 → 242	HOMO → LUMO	0.932	ILCT $^1\pi \rightarrow {}^1\pi^*$
	349	238 → 243	HOMO−3 → LUMO + 1	1.069	LLCT
		239 → 242			MLCT
		240 → 243	HOMO−2 → LUMO		$^1\pi \rightarrow {}^1\pi^*$
			HOMO−1 → LUMO + 1		
15–$P(CH_3)_3$	446	219 → 220	HOMO → LUMO	0.872	ILCT $^1\pi \rightarrow {}^1\pi^*$
	342	216 → 221	HOMO−3 → LUMO + 1	1.166	LLCT
		218 → 221			MLCT
			HOMO−1 → LUMO + 1		$^1\pi \rightarrow {}^1\pi^*$
	335	216 → 220	HOMO−3 → LUMO	0.248	ILCT
		219 → 221	HOMO−1 → HOMO + 1		$^1\pi \rightarrow {}^1\pi^*$

platinum metal centers are nonbonding versus antibonding in **4**–$P(CH_3)_3$ (Figure 6, right), which could account for the apparent differences in the measured quantum yields and calculated rate constants between **4** and **5a**. The LUMOs in both systems have antibonding character between the coordinating nitrogen and platinum metal center. This modulation of the energies of the HOMO and LUMO, with **5a**–$P(CH_3)_3$ (0.125 eV) having a larger energy gap than **4**–$P(CH_3)_3$ (0.119 eV), is in agreement with **4** having a lower-energy absorption band. It should be noted that the oscillator strengths of the lowest-energy predicted transitions from the calculations of **4** (0.925) and **5a** (0.715) reflect the trend observed in the experimental molar absorption coefficients of the low-energy optical transitions.

The predicted high-energy electronic transitions for **4**–$P(CH_3)_3$ and **5a**–$P(CH_3)_3$ were determined to originate from lower-lying occupied molecular orbitals [e.g., HOMO−5 for **4**–$P(CH_3)_3$ and HOMO−5 and HOMO−3 for **5a**–$P(CH_3)_3$] to unoccupied destination molecular orbitals that are higher than the LUMO [e.g., LUMO + 1 for **4**–$P(CH_3)_3$ and **5a**–$P(CH_3)_3$]. The observed optical transitions arising from the electronic transitions are predicted to occur at 343 nm for **4**–$P(CH_3)_3$ and 329 nm for **5a**–$P(CH_3)_3$. The molecular orbitals involved in the optical transition at 343 nm for **4**–$P(CH_3)_3$ show that the transition arises from the HOMO having the nitrogen p orbital and ethynyl π system in-phase and bonding, whereas the LUMO has little electron density on the aniline nitrogen p orbital and an antibonding ethynyl π system. Population analysis on the predicted high-energy electronic transition at 329 nm for **5a**–$P(CH_3)_3$ determined that the singlet transition arises from charge transfer from the Pt-aryl group to the ligand (>80% → <1%). Also, ca. 12% of the HOMO electron density lies on the Pt metal center for **5a**–$P(CH_3)_3$. In contrast, for the LUMO, more than 5% of the electron density is localized on the Pt metal centers; therefore, despite the mild ligand-to-metal charge-transfer (LMCT) character, the HOMO → LUMO transition appears to be more appropriately described as a ligand-to-ligand charge transfer (LLCT).

The TD-DFT calculations predict three electronic transitions to occur with oscillator strengths above 0.2 for **13**–$P(CH_3)_3$ (see Table 5). The predicted low-energy transition arises from an electron being promoted from the HOMO−2 to the LUMO, wherein the orbitals are largely ligand-centered (>95% electron density) and of π-type symmetry. The same electronic transition has a modest change in electron density on the

dx.doi.org/10.1021/ic400491q | Inorg. Chem. XXXX, XXX, XXX−XXX

platinum metal center (1.5% → 4.7%). A similar electronic transition was predicted at 455 nm for **14**−$P(CH_3)_3$, wherein the HOMO and LUMO are involved. The HOMO-to-LUMO transition involves π-type molecular orbitals with over 94% electron density being centered on the ligand, and it is accompanied by an increase in electron density on the platinum metal node (1.8% → 4.8%). This result is consistent with the previously discussed population analysis performed for **4**−$P(CH_3)_3$, wherein the ethynyl π system is weakened ($^1\pi \rightarrow {}^1\pi^*$) during the transition, with a loss of electron density on the aniline nitrogen.

A higher-energy optical transition with an oscillator strength of 1.316 that utilizes HOMO−5 and LUMO + 1 is predicted to occur at 343 nm for **13**−$P(CH_3)_3$. This is very similar in nature to the predicted lowest-energy transition where the molecular orbitals involved are of π-type symmetry and are ligand-centered with modest contributions from the metal center. HOMO−5 has 92% electron density on the ligand and 7.3% on the metal center. LUMO + 1 has 94% of its electron density centered on the ligand and 5.9% on the metal center.

The highest-energy predicted electronic transition for **13**−$P(CH_3)_3$ at 336 nm has an oscillator strength of 0.253. The electronic transition utilizes low-lying occupied (HOMO−2 and HOMO−5) and low-lying unoccupied (LUMO and LUMO + 1) molecular orbitals that were discussed in the previous predicted electronic transitions for **13**−$P(CH_3)_3$.

The high-energy electronic transition for **14**−$P(CH_3)_3$ is predicted to occur at 349 nm with an oscillator strength of 1.069 and, interestingly, can be characterized as a mixture of ligand−ligand (LLCT) and metal−ligand charge-transfer (MLCT) bands. For the occupied molecular orbitals predicted to be involved (HOMO−3, HOMO−2, and HOMO−1), a population analysis was performed on the Pt-phosphine metal center (22%), aryl ligand (46%), and ligand **1** (31%); the percentages represent the averages of the contributions for the molecular fragments. The destination molecular orbitals have 94.0% of the electron density on the ligand and 5.5% on the metal center. This predicted transition, however, is significantly different from those in **13**−$P(CH_3)_3$ and previously studied systems.

Pd system **15**−$P(CH_3)_3$ is predicted to have three electronic transitions with oscillator strengths over 0.20, with the lowest-energy state corresponding to an excitation at 446 nm. This electronic transition involves the HOMO and LUMO and consists of π-type molecular orbitals with >96% of the electron density centered on the ligand. A loss of electron density on the aniline nitrogen is accompanied by weakening of the ethynyl π system ($^1\pi \rightarrow {}^1\pi^*$) during the transition. A similar transition was observed for the highest-energy predicted transition at 335 nm.

The transition at 342 nm for **15**−$P(CH_3)_3$ involves HOMO−3 and HOMO−1 as the occupied molecular orbitals, with the destination unoccupied molecular orbital being LUMO + 1. During this transition, HOMO−1 has 73% of the electron density centered on the aryl group and 26.6% centered on Pd-phosphine. LUMO + 1 has 0.8% electron density on the aryl group and 5.4% on Pd-phosphine. This is a significant transfer of charge during the transition, unlike what is observed for the **4**−$P(CH_3)_3$ system, and is described as a mixture of LLCT and MLCT.

CONCLUSIONS

The photophysical properties of endohedral amine-functionalized bis(phosphine) Pt(II) SCCs can be tuned by using isomeric species. This is important because assembly reactions using isomeric donor ligands often do not require synthetic redesigns and therefore offer a way to alter the absorption and emission profiles of discrete SCCs without losing atom efficiency or changing synthetic conditions. Given the attractive photophysical properties observed for SCCs constructed from aniline-based donor ligands, developing a chemistry to tune these properties while maintaining the important aniline core is desirable. It was determined that the position of the coordinating nitrogen can greatly affect the photophysical properties of 2,6-diethynyl aniline-based ligands by using M−ligand−M fragments as suitable models for metallacyclic SCCs. The difference in the low-energy absorption bands was attributed to the different Pt−N coordination bonding modes in the HOMO. The M−ligand−M systems employed also allowed for this study to be extended to probing the metal fragment. Studies using functionalized aryl groups on the metal-based acceptor fragments showed no significant effects on the overall observed photophysical properties of the M−ligand−M systems despite having more significant charge-transfer mechanisms. Also, a Pd analogue, **15**, displayed an emission profile similar to that of its Pt counterpart, which suggests that less expensive systems employing bis(phosphine) Pd(II) nodes can be used in the synthesis of systems for photon-emitting devices without suffering a large penalty in the observed optical properties.

EXPERIMENTAL SECTION

Materials and Methods. 2,6-Bis(pyrid-4-ylethynyl) aniline[6] (**1**), 2,6-bis(pyrid-3-ylethynyl) aniline[7] (**2**), bromophenylbis(triethylphosphine)platinum,[20] μ-1,4-phenylenetetrakis(triethylphosphine)bis(1,1,1-trifluoromethanesulfonato-κO)diplatinum,[8] bromo(4-methoxy)bis(triethylphosphine)-, (*SP*-4-3)platinum (**10**),[9] iodo(4-nitrophenyl)bis(triethylphosphine)-, (*SP*-4-3) platinum (**11**),[10] and bromophenylbis(triethylphosphine) palladium (**12**)[11] were prepared using known procedures. All compounds were used as received from Sigma-Aldrich, Oakwood Chemicals, and TCI America, whereas deuterated solvents were purchased from Cambridge Isotope Laboratory (Andover, MA). ^{1}H and ^{31}P{^{1}H} NMR spectra were recorded on a Varian 300 spectrometer, and mass spectra were recorded on a Micromass LCT Premier XE time-of-flight (ToF) mass spectrometer using electrospray ionization and analyzed using the MassLynx software suite. The ESI-MS samples were dissolved in methylene chloride and then diluted with acetone unless otherwise noted. All ^{31}P{^{1}H} NMR spectra were referenced using a 10% H_3PO_4 (aq) solution. Elemental analysis was performed by Atlantic Microlab, Inc.

(1,1,1-Trifluoromethanesulfonato-κO)phenylbis(triethylphosphine)platinum (3). Bromophenylbis(triethylphosphine)platinum (99.5 mg, 169 μmol) and silver triflate (49.0 mg, 57.9 μmol) were weighed into a Schlenk flask, evacuated by reduced pressure, placed under N_2 atmosphere, and covered with aluminum foil. In another Schlenk flask, 10 mL of methylene chloride was degassed by the freeze−pump−thaw method. The methylene chloride was then transferred by cannula to the Schlenk flask containing the starting materials. The reaction mixture was allowed to stir at room temperature in the dark for 3 h. The resulting mixture was then filtered using air-free techniques. A clear, colorless solution was obtained, and after the methylene chloride had been removed by reduced pressure, an off-white solid was afforded; 88 mg (79% yield). ^{1}H NMR ($CDCl_3$, 300 MHz): δ 7.23 (d, 2H, ArH_α, J = 12.6 Hz), 6.85 (m, 3H, ArH), 1.61 (bs, 12H, PCH_2), 1.11 (m, 18H, PCH_3). ^{31}P{^{1}H} NMR (CD_2Cl_2, 121.4 MHz): δ 20.79 (bs; ^{195}Pt satellites, $^1J_{Pt-P}$ = 2847

dx.doi.org/10.1021/ic400491q | Inorg. Chem. XXXX, XXX, XXX−XXX

Hz). ESI-MS ($C_{19}H_{35}F_3O_3P_2PtS$) m/z: [M − OTf], 508.19; [M − OTf + acetone], 566.23. Anal. Calcd. for $C_{19}H_{35}F_3O_3P_2PtS$: C, 34.70; H, 5.36. Found: C, 34.85; H, 5.17.

General Procedure for the Synthesis of Pt-Aryl OTf-Capped Ligands. To a 2 dram vial was added 2,6-bis(pyrid-4-ylethynyl) aniline (**1**; 1.0 mg, 3.4 μmol) or 2,6-bis(pyrid-3-ylethynyl) aniline (**2**; 1.0 mg, 3.4 μmol) with (1,1,1-trifluoromethanesulfonato-κ*O*)-phenylbis(triethylphosphine)platinum (**3**; 4.5 mg, 6.8 μmol) in a 1:2 stoichiometric ratio. Deuterated methylene chloride (1 mL) was then added, and the mixture was allowed to stir for 3 h. The compound was then purified by precipitation upon addition of diethyl ether to the homogeneous solution. The mixture was centrifuged, and the supernatant was decanted.

Diphenyl{μ-[4,4′-(1-amino-2,6-ethynediylbenzene)]bis-(pyridine-κ*N*)}tetrakis(triethylphosphine)diplatinum (4). ^{1}H NMR ($CDCl_3$, 300 MHz): δ 8.56−8.60 (d, 4H, PyH_α, J = 12 Hz), 7.85−7.87 (d, 4H, PyH_β, J = 3 Hz), 7.49−7.52 (d, 2H, ArH, J = 9 Hz), 7.32−7.34 (d, 4H, PtArH_α, J = 6 Hz, J_{ArH-Pt} = 51 Hz), 7.05−7.09 (t, 4H, PtArH_β, J = 12 Hz), 6.95−6.97 (t, 2H, PtArH_γ, J = 6 Hz), 6.69−6.74 (t, 1H, ArH, J = 15 Hz), 5.83 (bs, 2H, ArNH_2), 1.31−1.35 (m, 24H, PCH_2), 1.07−1.17 (m, 36H, PCH_3). ^{31}P{^{1}H} NMR (CD_2Cl_2, 121.4 MHz): δ 10.84 (bs; ^{195}Pt satellites, $^1J_{Pt-P}$ = 2695 Hz). ESI-MS ($C_{58}H_{83}F_6N_3O_6P_4Pt_2S_2$) m/z: [M − OTf]$^+$, 1460.44; [M − 2OTf]$^{2+}$, 655.74. Anal. Calcd. for $C_{58}H_{83}F_6N_3O_6P_4Pt_2S_2$: C, 43.26; H, 5.19; N, 2.61. Found: C, 43.29; H, 5.23; N, 2.55.

Diphenyl{μ-[3,3′-(1-amino-2,6-ethynediylbenzene)]bis-(pyridine-κ*N*)}tetrakis(triethylphosphine)diplatinum (5a). ^{1}H NMR ($CDCl_3$, 300 MHz): δ 8.81 (s, 2H, PyH_α), 8.56−8.58 (d, 2H, Py$H_{\alpha'}$, J = 6 Hz), 8.30−8.32 (d, 2H, PyH_γ, J = 6 Hz), 7.68−7.73 (m, 2H, PyH_β), 7.48−7.50 (d, 2H, ArH, J = 6 Hz), 7.37−7.40 (d, 4H, PtArH_β, J = 9 Hz), 7.08 (m, 4H, PtArH_α), 6.98−7.01 (m, 2H, PtArH_γ), 6.69−6.75 (t, 1H, ArH, J = 18 Hz), 5.73 (bs, 2H, ArNH_2), 1.34 (m, 24H, PCH_2), 1.08−1.178 (m, 36H, PCH_3). ^{31}P{^{1}H} NMR (CD_2Cl_2, 121.4 MHz): δ 10.84 (bs; ^{195}Pt satellites, $^1J_{Pt-P}$ = 2695 Hz). ESI-MS ($C_{58}H_{83}F_6N_3O_6P_4Pt_2S_2$) m/z: [M − 2OTf]$^{2+}$, 655.74. Anal. Calcd for $C_{58}H_{83}F_6N_3O_6P_4Pt_2S_2$ [Complex]·CH_2Cl_2·Et_2O: C, 42.76; H, 5.41; N, 2.37. Found: C, 42.81; H, 5.22; N, 2.51.

Self-Assembly (6). In separate 2 dram vials, 1.0 mg (3.4 μmol) of 2,6-bis(pyrid-3-ylethynyl) aniline (**2**) and 3.4 mg (2.7 μmol) of μ-1,4-phenylenetetrakis(triethylphosphine)bis(1,1,1-trifluoromethanesulfonato-κ*O*)diplatinum were added. Each compound was then dissolved in 0.5 mL of deuterated methylene chloride. The μ-1,4-phenylenetetrakis(triethylphosphine)bis(1,1,1-trifluoromethanesulfonato-κ*O*)diplatinum solution was then added dropwise to a stirring solution of 2,6-bis(pyrid-3-ylethynyl) aniline, and the mixture was heated to 30 °C and allowed to stir for 48 h. After this step, the chartreuse-colored solution was filtered to remove any insoluble kinetic byproducts (i.e., polymers). The compound was then purified by precipitation upon addition of diethyl ether, centrifugation, and decantation of the supernatant (>85% yield). ^{1}H NMR ($CDCl_3$, 300 MHz): δ 9.10 (s, 4H, PyH_α), 8.58−8.60 (d, 4H, Py$H_{\alpha'}$, J = 6 Hz), 8.07−8.09 (d, 4H, PyH_γ, J = 6 Hz), 7.63−7.68 (m, 4H, PyH_β), 7.47−7.50 (d, 4H, ArH, J = 9 Hz), 7.21 (s, 4H, PtArH), 7.01 (s, 4H, PtArH), 6.68−6.73 (t, 2H, ArH, J = 15 Hz), 5.99 (bs, 4H, ArNH_2), 1.38 (m, 48H, PCH_2), 1.12−1.17 (m, 72H, PCH_3). ^{31}P{^{1}H} NMR (CD_2Cl_2, 121.4 MHz): δ 11.29 (bs; ^{195}Pt satellites, $^1J_{Pt-P}$ = 2730 Hz). ESI-MS ($C_{104}H_{154}F_{12}N_6O_{12}P_8Pt_4S_4$) m/z: [M − 2OTf]$^{2+}$, 1382.39; [M − 3OTf]$^{3+}$, 871.94. Anal. Calcd. for $C_{104}H_{154}F_{12}N_6O_{12}P_8Pt_4S_4$ [complex]: C, 40.76; H, 5.06; N, 2.74. Found: C, 41.09; H, 5.27; N, 3.07.

Diphenyl{μ-[4,4′-(1-amino-2,6-ethynediylbenzene)]bis-(pyridine-κN)}tetrakis(triethylphosphine)diplatinum (7). 2,6-Bis(pyrid-4-ylethynyl) aniline (**1**; 1.0 mg, 3.4 μmol) was weighed into a 2 dram vial. Two equivalents of each bromophenylbis-(triethylphosphine)platinum (4.0 mg, 6.8 μmol) and $AgNO_3$ (1.2 mg, 6.8 μmol) was also added to the same vial. CD_2Cl_2 (2 mL) was then added, and the mixture was stirred at room temperature for 48 h in the dark. The solution was then filtered twice with glass microfiber filters to remove insoluble AgBr; a green-colored solution of **7** was afforded (96% yield). ^{1}H NMR ($CDCl_3$, 300 MHz): δ 8.58−8.60 (d, 4H, PyH_α, J = 6 Hz), 7.90−7.92 (d, 4H, PyH_β, J = 6 Hz), 7.48−7.51 (d, 2H, ArH, J = 9 Hz), 7.31−7.34 (d, 4H, PtArH_α, J = 12 Hz, J_{ArH-Pt} = 24 Hz), 7.04−7.09 (t, 4H, PtArH_β, J = 15 Hz), 6.95−6.97 (t, 2H, PtArH_γ, J = 6 Hz), 6.66−6.71 (t, 1H, ArH, J = 15 Hz), 5.83 (bs, 2H, ArNH_2), 1.31−1.35 (m, 24H, PCH_2), 1.07−1.17 (m, 36H, PCH_3). ^{31}P{^{1}H} NMR (CD_2Cl_2, 121.4 MHz): δ 12.88 (bs; ^{195}Pt satellites, $^1J_{Pt-P}$ = 2696 Hz). ESI-MS ($C_{56}H_{83}N_5O_6P_4Pt_2$) m/z: [M − ONO_2]$^+$, 1373.47; [M − 2ONO_2]$^{2+}$, 655.74. Anal. Calcd. for $C_{56}H_{83}N_5O_6P_4Pt_2$: C, 46.83; H, 5.82; N, 4.88. Found: C, 47.08; H, 5.79; N, 5.26.

General Procedure for Synthesis of 13−15. Into a 2 dram vial was weighed 2,6-bis(pyrid-4-ylethynyl) aniline (**1**; 1 mg, 3.4 μmol) with bromo(4-methoxy)bis(triethylphosphine)-, (*SP*-4-3)platinum (**10**; 4.2 mg, 6.8 μmol), iodo(4-nitrophenyl)bis(triethylphosphine)-, (*SP*-4-3)platinum (**11**; 4.6 mg, 6.8 μmol), or bromophenylbis-(triethylphosphine) palladium (**12**; 3.4 mg, 6.8 μmol) in a 1:2 stoichiometric ratio. Two equivalents of AgOTf (1.7 mg, 6.8 μmol) was then added to the vial. CH_2Cl_2 (1 mL) was added, and the mixture was allowed to stir for 24 h in the dark at room temperature. The solution was then filtered and purified by precipitation upon addition of diethyl ether to the solution. The mixture was centrifuged, and the supernatant was decanted. The solid was redissolved in CD_2Cl_2 and characterized.

Platinum Methoxybenzene OTf-Capped Ligand (13). ^{1}H NMR ($CDCl_3$, 300 MHz): δ 8.56−8.58 (d, 4H, PyH_α, J = 6 Hz), 7.84−7.86 (d, 4H, PyH_β, J = 6 Hz), 7.49−7.51 (d, 2H, ArH, J = 6 Hz), 7.17−7.20 (d, 4H, PtArH_α, J = 9 Hz, J_{ArH-Pt} = 51 Hz), 6.71−6.74 (m, 5H, PtArH_β, ArH), 5.83 (bs, 2H, ArNH_2), 3.76 (s, 6H, OCH_3), 1.25−1.40 (m, 24H, PCH_2), 1.06−1.16 (m, 36H, PCH_3). ^{31}P{^{1}H} NMR (CD_2Cl_2, 121.4 MHz): δ 13.39 (bs; ^{195}Pt satellites, J_{Pt-P} = 2688 Hz). ESI-MS ($C_{60}H_{87}F_6N_3O_8P_4Pt_2S_2$) m/z: [M − OTf]$^+$, 1520.46; [M − 2OTf]$^{2+}$, 685.75. Anal. Calcd. for $C_{60}H_{87}F_6N_3O_8P_4Pt_2S_2$ [complex]·CH_2Cl_2·Et_2O: C, 42.67; H, 5.45; N, 2.30. Found: C, 42.58; H, 5.47; N, 2.48.

Platinum Nitrobenzene OTf-Capped Ligand (14). ^{1}H NMR ($CDCl_3$, 300 MHz): δ 8.58−8.60 (d, 4H, PyH_α, J = 6 Hz), 7.91−7.66 (m, 8H, PyH_β, Pt−ArH_β), 7.61−7.63 (d, 4H, Pt−ArH_α, J = 6 Hz), 7.50−7.53 (d, 2H, ArH, J = 9 Hz), 6.69−6.75 (t, 1H, ArH, J = 18 Hz), 5.83 (bs, 2H, ArNH_2), 1.28−1.39 (m, 24H, PCH_2), 1.06−1.19 (m, 36H, PCH_3). ^{31}P{^{1}H} NMR (CD_2Cl_2, 121.4 MHz): δ 11.98 (bs; ^{195}Pt satellites, J_{Pt-P} = 2597 Hz). ESI-MS ($C_{58}H_{81}F_6N_5O_{10}P_4Pt_2S_2$) m/z: [M − OTf]$^+$, 1550.36; [M − 2OTf]$^{2+}$, 700.69. Anal. Calcd. for $C_{58}H_{81}F_6N_5O_{10}P_4Pt_2S_2$: C, 40.97; H, 4.80; N, 4.12. Found: C, 41.14; H, 4.92; N, 4.03.

Palladium Benzene OTf-Capped Ligand (15). ^{1}H NMR ($CDCl_3$, 300 MHz): δ 8.52−8.54 (d, 4H, PyH_α, J = 6 Hz), 7.85−7.87 (d, 4H, PyH_β, J = 6 Hz), 7.48−7.50 (d, 2H, ArH, J = 6 Hz), 7.30−7.32 (d, 4H, Pd−ArH_β, J = 6 Hz), 7.11−7.15 (t, 4H, Pd−ArH_α, J = 12 Hz), 6.99−7.02 (t, 2H, Pd−ArH_γ, J = 9 Hz), 6.69−6.73 (t, 1H, ArH, J = 12 Hz), 5.78 (bs, 2H, ArNH_2), 1.28−1.39 (m, 24H, PCH_2), 1.06−1.19 (m, 36H, PCH_3). ^{31}P{^{1}H} NMR (CD_2Cl_2, 121.4 MHz): δ 6.78. ESI-MS ($C_{58}H_{83}F_6N_3O_6P_4Pd_2S_2$) m/z: [M − 2OTf]$^{2+}$, 567.68. Anal. Calcd. for $C_{58}H_{83}F_6N_3O_6P_4Pd_2S_2$: C, 48.61; H, 5.84; N, 2.93. Found: C, 48.50; H, 5.92; N, 2.95.

Steady-State Absorption and Emission Spectroscopy and Quantum Yield Determination. Absorption and fluorescence spectra were recorded on Hitachi U-4100 and Hitachi F-7000 spectrophotometers, respectively, with aerated spectrophotometric-grade methylene chloride (Sigma-Aldrich) at room temperature. The cells used in the experiments were 1-cm quartz cuvettes from Starna Cells, Inc. All samples were freshly prepared for each measurement. The molar absorption coefficients were determined by preparing four samples ranging in absorption from 0.01 to 1.0 with concentrations of 0.3−95 μM. The molar absorption coeffcient for each solution was then calculated using Beer's law, and the four values were averaged. Subsequent samples were then prepared to confirm the molar absorption coefficients. Quantum yields were determined by, first, cross-calibrating the instrument with quinine sulfate in 0.1 M H_2SO_4 and anthracene in ethanol. Quinine sulfate was then used to determine the experimental quantum yields at an excitation wavelength of 365 nm with Φ = 0.55. The quantum yield measurements were performed in multiplicates with values that were within 10% error being averaged.

dx.doi.org/10.1021/ic400491q | *Inorg. Chem.* XXXX, XXX, XXX−XXX

Excited-State Lifetime Measurement. Time-correlated single-photon-counting (TCSPC) experiments were performed on an IBH (Jobin Yvon Horiba) model 5000F instrument equipped with single monochromators on both the excitation and emission sides of the instrument. The excitation light source was a NanoLED with a short 800 ps pulse width at 336 nm (458 nm was also used for **13**–**15**). Emission signals were collected on a picosecond photon detection module (TBX-04) at an angle perpendicular to excitation for samples and blanks. Data were collected at the sample's peak maxima as determined by steady-state experiments and averaged (30000 counts) to obtain the decay profile. Decay analysis and curve fitting routines to determine the sample's lifetimes were performed by the software (DAS6) provided by the manufacturer (IBH). The instrument response for the setup used was determined to be 1 ns, and the error in the measurements was determined to be ±350 ps after deconvolution of the signal. The biexponential function that was utilized to calculate the excited-state lifetimes was $A(t) = A_1e^{-k_1t_1} + A_2e^{-k_2t_2}$.

Molecular Modeling. All calculations were performed using the Gaussian 09 program package, revision B.01,[19] with the Becke three-parameter hybrid exchange and the Lee–Yang–Parr correlation functionals (B3LYP).[16] The 6-31G** basis set[17] was used for H, C, N, and P atoms, whereas the Los Alamos National Laboratories (LANL2DZ)[18] basis set and pseudopotential was used for Pt and Pd. All geometry optimizations were performed without a solvent field with C_1 symmetry; the results are for the gas phase. To minimize computational cost, the PEt_3 ligands on Pt and Pd were modeled as $P(CH_3)_3$ ligands. Orbitals were visualized using Chem3D and GaussView 5.0 with an isovalue of 0.02.

The percentages of platinum, palladium, phosphine, platinum-aryl, and ligand character in the occupied (canonical) molecular orbitals (MOs) and virtual orbitals discussed for the previous complexes were calculated from a full population analysis, using the equation

$$\text{orbital character}_{(\text{Pt or Pd,Pt–Ar,phosphine,lig})}\,(\%) = \frac{\sum \varphi_{(\text{Pt or Pd,Pt–Ar,phosphine,lig})}^{2}}{\sum \varphi_{(\text{all})}^{2}} \times 100\%$$

where $\sum\varphi_i$ (i = Pd, Pt, Pt–Ar, phosphine, lig, or all) is the sum of the squares of the eigenvalues associated with the atomic orbital (AO) of interest or all of the AOs in a particular MO. The vertical singlet transition energies of the complexes were computed by time-dependent density functional theory using Gaussian 09 with the ground-state optimized structure.

■ ASSOCIATED CONTENT

Ⓢ Supporting Information

^1H and $^{31}P\{^1H\}$ NMR spectra, steady-state absorption and emission spectra of **2**, excited-state lifetime decay profiles, electrospray ionization mass spectrometry spectra, atomic coordinates from DFT, and all electronic transitions from TD-DFT with nonzero oscillator strengths. This material is available free of charge via the Internet at http://pubs.acs.org.

■ AUTHOR INFORMATION

Corresponding Author

*E-mail: bryant@chem.utah.edu (J.B.P.), Stang@chem.utah.edu (P.J.S.).

Notes

The authors declare no competing financial interest.

■ ACKNOWLEDGMENTS

P.J.S. thanks the NSF (NSF-CHE 0820955) for financial support. We also thank the Center for High Performance Computing (CHPC) at the University of Utah for access and time allotment to perform the DFT and TD-DFT calculations. D.A.L. was sponsored by the Division of Chemical Sciences, Geosciences and Biosciences, Office of Basic Energy Sciences, U.S. Department of Energy.

■ REFERENCES

(1) (a) Caulder, D. L.; Brückner, C.; Powers, R. E.; König, S.; Parac, T. N.; Leary, J. A.; Raymond, K. N. *J. Am. Chem. Soc.* **2001**, *123*, 8923. (b) Caulder, D. L.; Raymond, K. N. *Acc. Chem. Res.* **1999**, *32*, 975. (c) Gianneschi, N. C.; Masar, M. S.; Mirkin, C. A. *Acc. Chem. Res.* **2005**, *38*, 825. (d) Farha, O. K.; Hupp, J. T. *Acc. Chem. Res.* **2010**, *43*, 1166. (e) Lee, J.; Farha, O. K.; Roberts, J.; Scheidt, K. A.; Nguyen, S. T.; Hupp, J. T. *Chem. Soc. Rev.* **2009**, 38. (f) Fujita, M. *Chem. Soc. Rev.* **1998**, *27*, 417. (g) Fujita, M.; Tominaga, M.; Hori, A.; Therrien, B. *Acc. Chem. Res.* **2005**, *38*, 369. (h) Cotton, F. A.; Lin, C.; Murillo, C. A. *Acc. Chem. Res.* **2001**, *34*, 759. (i) Cotton, F. A.; Lin, C.; Murillo, C. A. *Proc. Natl. Acad. Sci. U.S.A.* **2002**, *99*, 4810. (j) Chakrabarty, R.; Mukherjee, P. S.; Stang, P. J. *Chem. Rev.* **2011**, *111*, 6810. (k) Ghosh, S.; Mukherjee, P. S. *Organometallics* **2008**, *27*, 316. (l) Vajpayee, V.; Kim, H.; Mishra, A.; Mukherjee, P. S.; Stang, P. J.; Lee, M. H.; Kim, H. K.; Chi, K.-W. *Dalton Trans.* **2011**, *40*, 3112. (m) De, S.; Mahata, K.; Schmittel, M. *Chem. Soc. Rev.* **2010**, 39. (n) Safont-Sempere, M. M.; Fernández, G.; Würthner, F. *Chem. Rev.* **2011**, *111*, 5784.

(2) (a) Stang, P. J.; Olenyuk, B. *Acc. Chem. Res.* **1997**, *30*, 502. (b) Barry, N. P. E.; Edafe, F.; Dyson, P. J.; Therrien, B. *Dalton Trans.* **2010**, *39*, 2816. (c) Barry, N. P. E.; Edafe, F.; Therrien, B. *Dalton Trans.* **2011**, *40*, 7172. (d) Barry, N. P. E.; Therrien, B. *Eur. J. Inorg. Chem.* **2009**, *2009*, 4695. (e) Barry, N. P. E.; Zava, O.; Furrer, J.; Dyson, P. J.; Therrien, B. *Dalton Trans.* **2010**, *39*, 5272. (f) Cook, T. R.; Zheng, Y.-R.; Stang, P. J. *Chem. Rev.* **2012**, *113*, 734. (g) Leininger, S.; Olenyuk, B.; Stang, P. J. *Chem. Rev.* **2000**, *100*, 853.

(3) (a) Flynn, D. C.; Ramakrishna, G.; Yang, H.-B.; Northrop, B. H.; Stang, P. J.; Goodson, T. *J. Am. Chem. Soc.* **2010**, *132*, 1348. (b) Zhao, G.-J.; Yu, F.; Zhang, M.-X.; Northrop, B. H.; Yang, H.; Han, K.-L.; Stang, P. J. *J. Phys. Chem. A* **2011**, *115*, 6390. (c) Zhao, G.-J.; Northrop, B. H.; Han, K.-L.; Stang, P. J. *J. Phys. Chem. A* **2010**, *114*, 9007. (d) Zhao, G.-J.; Northrop, B. H.; Stang, P. J.; Han, K.-L. *J. Phys. Chem. A* **2010**, *114*, 3418. (e) Chen, J.-S.; Zhao, G.-J.; Cook, T. R.; Sun, X.-F.; Yang, S.-Q.; Zhang, M.-X.; Han, K.-L.; Stang, P. J. *J. Phys. Chem. A* **2012**, *116*, 9911. (f) Chen, J.-S.; Zhao, G.-J.; Cook, T. R.; Han, K.-L.; Stang, P. J. *J. Am. Chem. Soc.* **2013**, *135*, 6694.

(4) (a) Wong, K. M.-C.; Yam, V. W.-W. *Coord. Chem. Rev.* **2007**, *251*, 2477. (b) Eryazici, I.; Moorefield, C. N.; Newkome, G. R. *Chem. Rev.* **2008**, *108*, 1834. (c) Fleischauer, P. D.; Fleischauer, P. *Chem. Rev.* **1970**, *70*, 199. (d) Kindahl, T.; Ellingsen, P. G.; Lopes, C.; Brännlund, C.; Lindgren, M.; Eliasson, B. *J. Phys. Chem. A* **2012**, *116*, 11519. (e) Chan, K. H.-Y.; Chow, H.-S.; Wong, K. M.-C.; Yeung, M. C.-L.; Yam, V. W.-W. *Chem. Sci.* **2010**, *1*, 477. (f) Hui, C.-K.; Chu, B. W.-K.; Zhu, N.; Yam, V. W.-W. *Inorg. Chem.* **2002**, *41*, 6178. (g) Wong, K. M.-C.; Yam, V. W.-W. *Acc. Chem. Res.* **2011**, *44*, 424. (h) Adamson, A. W.; Waltz, W. L.; Zinato, E.; Watts, D. W.; Fleischauer, P. D.; Lindholm, R. D. *Chem. Rev.* **1968**, *68*, 541. (i) Brooks, J.; Babayan, Y.; Lamansky, S.; Djurovich, P. I.; Tsyba, I.; Bau, R.; Thompson, M. E. *Inorg. Chem.* **2002**, *41*, 3055. (j) Caspar, J. V. *J. Am. Chem. Soc.* **1985**, *107*, 6718. (k) Chan, S.-C.; Chan, M. C. W.; Wang, Y.; Che, C.-M.; Cheung, K.-K.; Zhu, N. *Chem.—Eur. J.* **2001**, *7*, 4180. (l) Pomestchenko, I. E.; Luman, C. R.; Hissler, M.; Ziessel, R.; Castellano, F. N. *Inorg. Chem.* **2003**, *42*, 1394. (m) Danilov, E. O.; Rachford, A. A.; Goeb, S. b.; Castellano, F. N. *J. Phys. Chem. A* **2009**, *113*, 5763. (n) Goeb, S.; Prusakova, V.; Wang, X.; Vezinat, A.; Salle, M.; Castellano, F. N. *Chem. Commun.* **2011**, *47*, 4397. (o) Forniés, J.; Fuertes, S.; Martín, A.; Sicilia, V.; Lalinde, E.; Moreno, M. T. *Chem.—Eur. J.* **2006**, *12*, 8253. (p) Keller, J. M.; Glusac, K. D.; Danilov, E. O.; McIlroy, S.; Sreearuothai, P.; R. Cook, A.; Jiang, H.; Miller, J. R.; Schanze, K. S. *J. Am. Chem. Soc.* **2011**, *133*, 11289. (q) Keller, J. M.; Schanze, K. S. *Organometallics* **2009**, *28*, 4210. (r) Liao, C.; Yarnell, J. E.; Glusac, K. D.; Schanze, K. S. *J. Phys. Chem. B* **2010**, *114*, 14763. (s) Rogers, J. E.; Slagle, J. E.; Krein, D. M.; Burke, A. R.; Hall, B. C.; Fratini, A.; McLean, D. G.; Fleitz, P. A.; Cooper, T. M.; Drobizhev, M.;

Makarov, N. S.; Rebane, A.; Kim, K.-Y.; Farley, R.; Schanze, K. S. *Inorg. Chem.* **2007**, *46*, 6483.
(5) Kryschenko, Y. K.; Seidel, S. R.; Arif, A. M.; Stang, P. J. *J. Am. Chem. Soc.* **2003**, *125*, 5193.
(6) Pollock, J. B.; Cook, T. R.; Stang, P. J. *J. Am. Chem. Soc.* **2012**, *134*, 10607.
(7) Johnson, A. M.; Moshe, O.; Gamboa, A. S.; Langloss, B. W.; Limtiaco, J. F. K.; Larive, C. K.; Hooley, R. J. *Inorg. Chem.* **2011**, *50*, 9430.
(8) Manna, J.; Kuehl, C. J.; Whiteford, J. A.; Stang, P. J.; Muddiman, D. C.; Hofstadler, S. A.; Smith, R. D. *J. Am. Chem. Soc.* **1997**, *119*, 11611.
(9) Arnold, D. P.; Bennett, M. A. *Inorg. Chem.* **1984**, *23*, 2117.
(10) Tam, W.; Calabrese, J. C. *Chem. Phys. Let.* **1988**, *144*, 79.
(11) Calvin, G.; Coates, G. E. *J. Chem. Soc.* **1960**, *0*, 2008.
(12) (a) Yang, J.-S. In *PATAI'S Chemistry of Functional Groups*; John Wiley & Sons: New York, 2009, 10.1002/9780470682531.pat0396. (b) Hou, X.-J.; Quan, P.; Höltzl, T.; Veszprémi, T.; Nguyen, M. T. *J. Phys. Chem. A* **2005**, *109*, 10396. (c) Lewis, F. D.; Hougland, J. L.; Markarian, S. A. *J. Phys. Chem. A* **2000**, *104*, 3261. (d) Oosterbaan, W. D.; Koeberg, M.; Piris, J.; Havenith, R. W. A.; van Walree, C. A.; Wegewijs, B. R.; Jenneskens, L. W.; Verhoeven, J. W. *J. Phys. Chem. A* **2001**, *105*, 5984. (e) Rückert, I.; Demeter, A.; Morawski, O.; Kühnle, W.; Tauer, E.; Zachariasse, K. A. *J. Phys. Chem. A* **1999**, *103*, 1958.
(13) (a) Kohler, A.; Wilson, J. S.; Friend, R. H.; Al-Suti, M. K.; Khan, M. S.; Gerhard, A.; Bassler, H. *J. Chem. Phys.* **2002**, *116*, 9457. (b) Ricciardi, L.; Puoci, F.; Cirillo, G.; La Deda, M. *Dalton Trans.* **2012**, *41*, 10923.
(14) Weil, T. A.; Schmidt, P. J.; Rycheck, M.; Orchin, M. *Inorg. Chem.* **1969**, *8*, 1002.
(15) Vrieze, K.; Volger, H. C.; Gronert, M.; Praat, A. P. *J. Organomet. Chem.* **1969**, *16*, P19.
(16) (a) Becke, A. D. *J. Chem. Phys.* **1993**, *98*, 5648. (b) Lee, C.; Yang, W.; Parr, R. G. *Phys. Rev. B* **1988**, *37*, 785.
(17) Hehre, W. J.; Ditchfield, R.; Pople, J. A. *J. Chem. Phys.* **1972**, *56*, 2257.
(18) Hay, P. J.; Wadt, W. R. *J. Chem. Phys.* **1985**, *82*, 299.
(19) Frisch, M. J.; Trucks, G. W.; Schlegel, H. B.; Scuseria, G. E.; Robb, M. A.; Cheeseman, J. R.; Scalmani, G.; Barone, V.; Mennucci, B.; Petersson, G. A.; Nakatsuji, H.; Caricato, M.; Li, X.; Hratchian, H. P.; Izmaylov, A. F.; Bloino, J.; Zheng, G.; Sonnenberg, J. L.; Hada, M.; Ehara, M.; Toyota, K.; Fukuda, R.; Hasegawa, J.; Ishida, M.; Nakajima, T.; Honda, Y.; Kitao, O.; Nakai, H.; Vreven, T.; Montgomery, J. A., Jr.; Peralta, J. E.; Ogliaro, F.; Bearpark, M.; Heyd, J. J.; Brothers, E.; Kudin, K. N.; Staroverov, V. N.; Keith, T.; Kobayashi, R.; Normand, J.; Raghavachari, K.; Rendell, A.; Burant, J. C.; Iyengar, S. S.; Tomasi, J.; Cossi, M.; Rega, N.; Millam, J. M.; Klene, M.; Knox, J. E.; Cross, J. B.; Bakken, V.; Adamo, C.; Jaramillo, J.; Gomperts, R.; Stratmann, R. E.; Yazyev, O.; Austin, A. J.; Cammi, R.; Pomelli, C.; Ochterski, J. W.; Martin, R. L.; Morokuma, K.; Zakrzewski, V. G.; Voth, G. A.; Salvador, P.; Dannenberg, J. J.; Dapprich, S.; Daniels, A. D.; Farkas, Ö.; Foresman, J. B.; Ortiz, J. V.; Cioslowski, J.; Fox, D. J. *Gaussian 09*, revision C.01; Gaussian, Inc.: Wallingford, CT, 2010.
(20) Rieke, R. D.; Kavaliunas, A. V. *J. Org. Chem.* **1979**, *44*, 3069.

dx.doi.org/10.1021/ic400491q | *Inorg. Chem.* XXXX, XXX, XXX−XXX